

Materials Science

Geometric configuration of polyhedrons dominating particle- to wave-like thermal transport in single crystalline Cs₃Bi₂I₉

Linjie Wu¹, Zhiwei Chen^{1,*}, Qingyu Bai¹, Ziyue Liu¹, Yueyue Cheng¹, Te Kang¹, Changyuan Li¹, Hui Bu², Jun Luo^{1,*} & Yanzhong Pei^{1,*}

¹Interdisciplinary Materials Research Center, School of Materials Science and Engineering, Tongji University, Shanghai 201804, China;

²Hefei Govisionox Technology Co., Ltd., Hefei 230000, China

*Corresponding authors (emails: 14czw@tongji.edu.cn (Zhiwei Chen); junluo@tongji.edu.cn (Jun Luo); yanzhong@tongji.edu.cn (Yanzhong Pei))

Received 16 September 2025; Revised 26 October 2025; Accepted 29 October 2025; Published online 30 October 2025

Abstract: The thermal transport in a lattice is governed by the structural chemistry, which is critically important for heat flux management in thermoelectric conversion. Here, we reveal the structural chemistry origin that determines the thermal transport behavior and the marked anisotropy in single-crystalline Cs₃Bi₂I₉. Along the crystallographic *c*-axis direction, the particle-behavior-dominated thermal conductivity (κ) is approximately 0.3 W/(m K) at room temperature and decreases with increasing temperature. In contrast, the thermal transport perpendicular to the *c*-direction is primarily wave-like behavior, exhibiting a room-temperature κ of 0.17 W/(m K) that increases at elevated temperatures. This fundamental difference in thermal transport mechanisms arises from distinct chemical bonding environments, specifically the strong binding force between the face-sharing [BiI₆] octahedrons parallel to the *c*-direction and the weak rattling behavior between corner-sharing [CsI₁₂] cuboctahedrons perpendicular to the *c*-direction. These findings provide a design principle for manipulating thermal transport through crystal chemistry engineering, opening avenues for developing anisotropic thermoelectric materials with thermal management capabilities.

Keywords: bismuth halide perovskite, anisotropic thermal conductivity, thermal transport mechanisms

INTRODUCTION

Halide perovskites with low thermal conductivity have attracted increasing attention in thermal management [1–3] and thermoelectric conversion [4,5], due to their unique structural properties and lattice dynamics [6–8]. By suppressing heat conduction, these materials have the potential to extend the lifespan of equipment and promote the development of high-efficiency energy conversion technologies [9]. Lead-free metal halides have emerged as ideal candidates for thermal management, offering tunable structures, excellent optoelectronic properties, good stability, and environmentally friendly characteristics [10,11]. Among these properties, low thermal conductivity is an important indicator for achieving efficient thermal management [12–14].

Recently, Biswas *et al.* [15] reported an all-inorganic halide perovskite Cs₃Bi₂I₉ with thermal conductivity (κ) as low as 0.2 W/(m K). Thus, it is considered one of the most promising candidates for thermoelectrics and has attracted extensive research interests in recent years. For instance, the thermal transport properties of

$\text{Cs}_3\text{Bi}_2\text{I}_9$ and BiI_3 have been investigated by the time-domain thermo-reflectance technique [16]. The results reveal that $\text{Cs}_3\text{Bi}_2\text{I}_9$ thin films exhibit a substantially lower κ of 0.15 W/(m K) compared to BiI_3 thin films with κ of 0.31 W/(m K). Reducing the grain size can further reduce the thermal conductivity of $\text{Cs}_3\text{Bi}_2\text{I}_9$ [17]. The results demonstrate that when the grain size decreases from 200 to 20 nm, the room-temperature thermal conductivity drops from 0.25 to 0.18 W/(m K). More importantly, the enhanced grain boundary scattering weakens the temperature dependence of thermal conductivity.

Intrinsically, the change of temperature dependence of κ is described by the complex interplay between particle-like and wave-like transport mechanisms [18–20]. In crystalline materials, heat carriers exhibit particle-like collisions governed by the Boltzmann transport equation [21]. Conversely, in glasses, heat carriers display wave-like coherence via Zener tunneling between quadratically coupled vibrational eigenstates, as formalized in the Allen-Feldman equation [22]. The temperature dependence of thermal conductivity is the critical indicator of these microscopic mechanisms. The dominance of either particle-like or wave-like transport is fundamentally determined by a material's structural chemistry, which governs the phonon scattering pathways and the degree of wave localization [23,24].

For particle-like dominated phonon transport in $\text{K}_2\text{Ag}_4\text{Se}_3$, Li *et al.* [25] reported that the Ag atoms display rattling-like vibrations, inducing low-frequency phonon softening and enhanced anharmonicity. The long-range Se-Se interactions cause high-frequency optical branch softening. The $[\text{AgSe}_3]$ structural units simultaneously suppress both particle-like collisions and wave-like coherence of phonons, leading to significantly reduced thermal conductivity. Similarly, Xiong *et al.* [18] reported a particle-dominated thermal transport mechanism in $\text{X}_6\text{Re}_6\text{S}_8\text{I}_8$ (X=Rb/Cs). The interplay between the strongly covalent $[\text{Re}_6\text{S}_8\text{I}_6]^{4-}$ clusters and the weakly ionic framework formed by $\text{Rb}^+/\text{Cs}^+-\text{I}^-$ induces phonon band flattening and low-frequency phonon localization. The resulting phonon flat bands significantly enhance anharmonicity, enabling the ultralow thermal conductivity below 0.2 W/(m K).

For wave-like dominated transport in Cu_7PS_6 , Shen *et al.* [20] revealed that the wave-like ultralow thermal conductivity originates from the low-temperature cubic $P2_13$ phase. The crystal structure comprises a $[\text{PS}_4]^{3-}$ tetrahedral framework, which incorporates a four-coordination Cu-S tetrahedron and a five-coordination Cu-S polyhedron. Computational results further elucidate that this wave-dominated thermal transport primarily arises from the contribution of low-energy overlapping optical phonons associated with copper atoms. For an all-inorganic halide perovskite $\text{Cs}_3\text{Bi}_2\text{Br}_9$, Li *et al.* [26] reported that the crystal structure features an alternating stack of $[\text{Bi}_2\text{Br}_9]^{3-}$ layers and Cs^+ ions. The wave-like thermal conductivity originates from the suppressed heat transport by acoustic phonons and from the increased contribution of optical phonons through coherent transport. Chen *et al.* [27] reported stronger wave-like phonon transport along the *a*-axis and stronger particle-like phonon transport along the *c*-axis in KCu_7S_4 . These results demonstrate that the conventional anisotropy of lattice thermal conductivity could be altered through the construction of polycrystalline textured materials.

The diverse geometry configurations of polyhedral in $\text{Cs}_3\text{Bi}_2\text{I}_9$ make it an ideal material for investigating the structural chemistry origin of particle-like and wave-like thermal transport phenomena. Although the previous results reported preliminary κ values for the polycrystalline $\text{Cs}_3\text{Bi}_2\text{I}_9$ [15], the effect of microstructures naturally existing in polycrystalline materials on heat insulation behavior cannot be ruled out. $\text{Cs}_3\text{Bi}_2\text{I}_9$ crystallizes in a highly anisotropic hexagonal crystal structure with the space group $P63/mmc$. The lattice includes Cs atoms occupying two distinct positions (Wyckoff 2b and 4f), Bi atoms located at a single

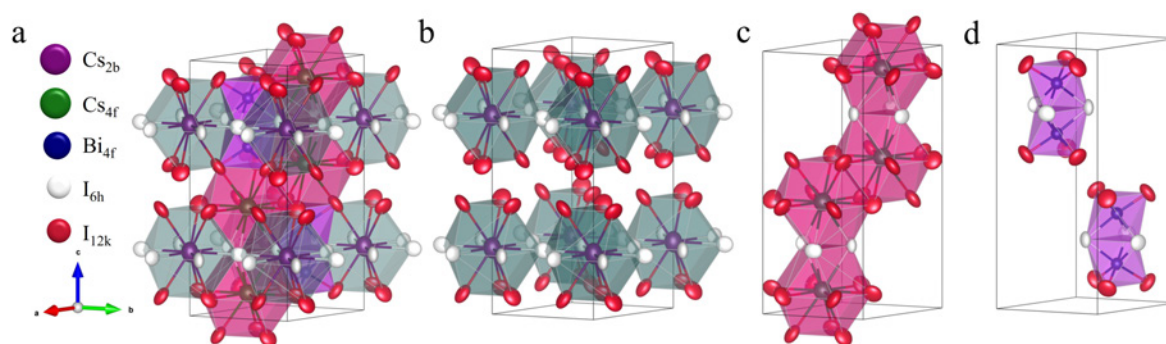


Figure 1 (a) Room-temperature crystal structure of $\text{Cs}_3\text{Bi}_2\text{I}_9$ indexing the hexagonal $P63/mmc$ phase. Local coordination environments for corner-sharing $[\text{CsI}_{12}]$ cuboctahedrons (b), face-sharing $[\text{CsI}_{12}]$ cuboctahedrons (c), and face-sharing $[\text{BiI}_6]$ octahedrons (d).

site (Wyckoff 4f), and I atoms occupying two distinct sites (Wyckoff 6h and 12k). Specifically, the Cs_{2b} and Cs_{4f} (the subscript here denotes the Wyckoff site) coordinate with the adjacent I_{12k} and I_{6h} atoms, forming the corner-sharing and face-sharing cuboctahedrons, respectively. Centrally located Bi_{4f} atoms bond with surrounding I_{12k} and I_{6h} atoms, where two $[\text{BiI}_6]$ octahedra connect through face-sharing, forming a $[\text{Bi}_2\text{I}_9]^{3-}$ dimer.

In this work, we synthesized polycrystalline samples using the high-temperature melting method and grew single crystals via the vertical gradient freezing method. The material exhibits distinct thermal conductivity values along different crystallographic axes, approximately 0.29 W/(m K) parallel to the c -direction and 0.17 W/(m K) perpendicular to the c -direction. The strong binding forces between the face-sharing $[\text{CsI}_{12}]$ cuboctahedrons and $[\text{BiI}_6]$ octahedrons facilitate the particle-like transport parallel to the c -direction, while the weak rattling behavior in corner-sharing $[\text{CsI}_{12}]$ cuboctahedrons and localized rattling motion of Cs_{2b} atoms indicate predominantly wave-like transport perpendicular to the c -direction.

RESULTS AND DISCUSSION

The crystal structure of $\text{Cs}_3\text{Bi}_2\text{I}_9$ obtained from single-crystal X-ray diffraction (XRD) refinement is shown in Figure 1a, revealing lattice parameters of $a=b=8.38 \text{ \AA}$ and $c=21.11 \text{ \AA}$, which are in good agreement with previously reported data [28]. The detailed refinement parameters are shown in Table 1. The hexagonal $P63/mmc$ phase of $\text{Cs}_3\text{Bi}_2\text{I}_9$ contains three types of polyhedrons. Figure 1b displays eight corner-sharing twelve-coordination cuboctahedrons within the unit cell, each polyhedron consisting of one Cs_{2b} , six I_{6h} and six I_{12k} atoms. The bonding environment consists of six $\text{Cs}_{2b}\text{-I}_{6h}$ bonds (4.19 Å) and six $\text{Cs}_{2b}\text{-I}_{12k}$ bonds (4.29 Å). Figure 1c illustrates four similar twelve-coordination cuboctahedrons, with a bonding environment of three $\text{Cs}_{4f}\text{-I}_{6h}$ bonds (4.25 Å) and nine $\text{Cs}_{4f}\text{-I}_{12k}$ bonds (4.19/4.21 Å). This series of face-sharing cuboctahedrons is parallel to the c -direction. As depicted in Figure 1d, the unit cell contains two six-coordination octahedra $[\text{BiI}_6]$ consisting of one Bi_{4f} , three I_{6h} , and three I_{12k} atoms, with bond lengths of three $\text{Bi}_{4f}\text{-I}_{6h}$ bonds (3.23 Å) and three $\text{Bi}_{4f}\text{-I}_{12k}$ bonds (2.93 Å), respectively. Two of these octahedra constitute a $[\text{Bi}_2\text{I}_9]^{3-}$ dimer through face-sharing parallel to the c -direction. The shapes of the thermal vibration ellipsoids of the I_{6h} and I_{12k} atoms qualitatively reflect the inter-atomic binding force, where the anisotropic atomic

Table 1 Crystallographic information from single-crystal XRD refinements at 300 K

Parameters	Values
Formula	Cs ₃ Bi ₂ I ₉
Molar mass (g/mol)	1958.79
Crystal size (mm ³)	0.04×0.08×0.12
Crystal system	Hexagonal
Space group	<i>P63/mmc</i>
<i>T</i> (K)	300
<i>a</i> (Å)	8.3793(2)
<i>b</i> (Å)	8.3793(2)
<i>c</i> (Å)	21.1104(10)
α (°)	90
β (°)	90
γ (°)	120
<i>V</i> (Å ³)	1283.64
<i>Z</i>	2
<i>D</i> _{calcd} (kg/m ³)	5.068
<i>F</i> (000)	1616
μ (mm ⁻¹)	28.686
θ range (°)	2.81–27.39
Reflections collected	5838
Independent reflections (<i>R</i> _{int})	607
Reflections observed [<i>I</i> > 2σ(<i>I</i>)]	597
Data/restraints/parameters	607/0/19
<i>R</i> ₁ , <i>wR</i> ₂ (<i>I</i> > 2σ(<i>I</i>))	0.0416, 0.0861
<i>R</i> ₁ , <i>wR</i> ₂ (all data)	0.0427, 0.0865
Goof on <i>F</i> ²	1.297
$\Delta\rho_{\max}$, $\Delta\rho_{\min}$ (e/Å ³)	2.444/−2.280
Position <i>x/y/z</i> of Cs _{2b}	0.00000/0.00000/0.25000
Position <i>x/y/z</i> of Cs _{4f}	0.66667/0.33333/0.41869
Position <i>x/y/z</i> of Bi _{4f}	0.33333/0.66667/0.34548
Position <i>x/y/z</i> of I _{6h}	0.50746/0.49254/0.25000
Position <i>x/y/z</i> of I _{12k}	0.66667/0.33333/0.41869
Mean-square displacements <i>U</i> ₁₁ / <i>U</i> ₂₂ / <i>U</i> ₃₃ / <i>U</i> ₁₂ / <i>U</i> ₁₃ / <i>U</i> ₂₃ of Cs _{2b} (Å ²)	0.0423/0.0423/0.0625/0/0/0.0212
Mean-square displacements <i>U</i> ₁₁ / <i>U</i> ₂₂ / <i>U</i> ₃₃ / <i>U</i> ₁₂ / <i>U</i> ₁₃ / <i>U</i> ₂₃ of Cs _{4f} (Å ²)	0.0468/0.0468/0.0477/0/0/0.0234
Mean-square displacements <i>U</i> ₁₁ / <i>U</i> ₂₂ / <i>U</i> ₃₃ / <i>U</i> ₁₂ / <i>U</i> ₁₃ / <i>U</i> ₂₃ of Bi _{4f} (Å ²)	0.0203/0.0203/0.0219/0/0/0.01016
Mean-square displacements <i>U</i> ₁₁ / <i>U</i> ₂₂ / <i>U</i> ₃₃ / <i>U</i> ₁₂ / <i>U</i> ₁₃ / <i>U</i> ₂₃ of I _{6h} (Å ²)	0.0379/0.0379/0.0384/0/0/0.0300
Mean-square displacements <i>U</i> ₁₁ / <i>U</i> ₂₂ / <i>U</i> ₃₃ / <i>U</i> ₁₂ / <i>U</i> ₁₃ / <i>U</i> ₂₃ of I _{12k} (Å ²)	0.0341/0.0483/0.0459/0.0097/0.0195/0.0170

displacement parameters (*U*) between Bi and I are much smaller than those between Cs and I, as listed in Table 1.

The XRD patterns of Cs₃Bi₂I₉ single-crystalline and polycrystalline samples are shown in Figure 2a, all diffraction peaks index the hexagonal crystal structure (ICSD#410726) with no impurity peaks observed. The lattice structure is consistent with the results reported in reference [15]. As shown in Figure 2b, the rocking curve analysis shows that the (006) diffraction peak exhibits a wide full width at half maximum (FWHM) of 0.47°, indicating the existence of lattice defects. Xu *et al.* [29] investigated these point defects by calculating the defect formation energies and transition energy levels. The article provides a detailed list of the formation energies of intrinsic point defects in various perovskite materials, such as MAPbI₃, FAPbI₃, and CsPbBr₃. For

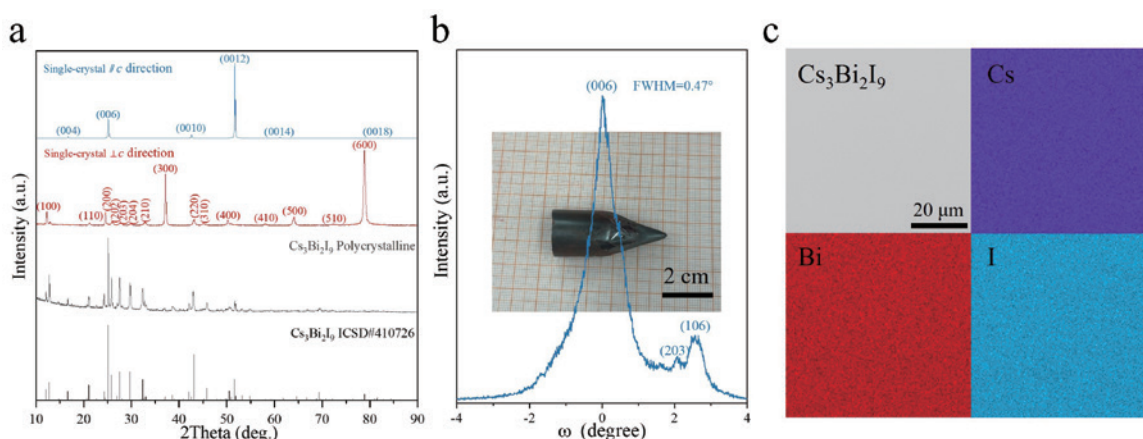


Figure 2 (a) X-ray diffraction (XRD) pattern of single-crystal and polycrystalline $\text{Cs}_3\text{Bi}_2\text{I}_9$. (b) High-resolution XRD rocking curve of the (006) diffraction peak and the optical photograph of single-crystal $\text{Cs}_3\text{Bi}_2\text{I}_9$ (inset). (c) Scanning electron microscope (SEM) image and corresponding EDS mappings for the single-crystal $\text{Cs}_3\text{Bi}_2\text{I}_9$.

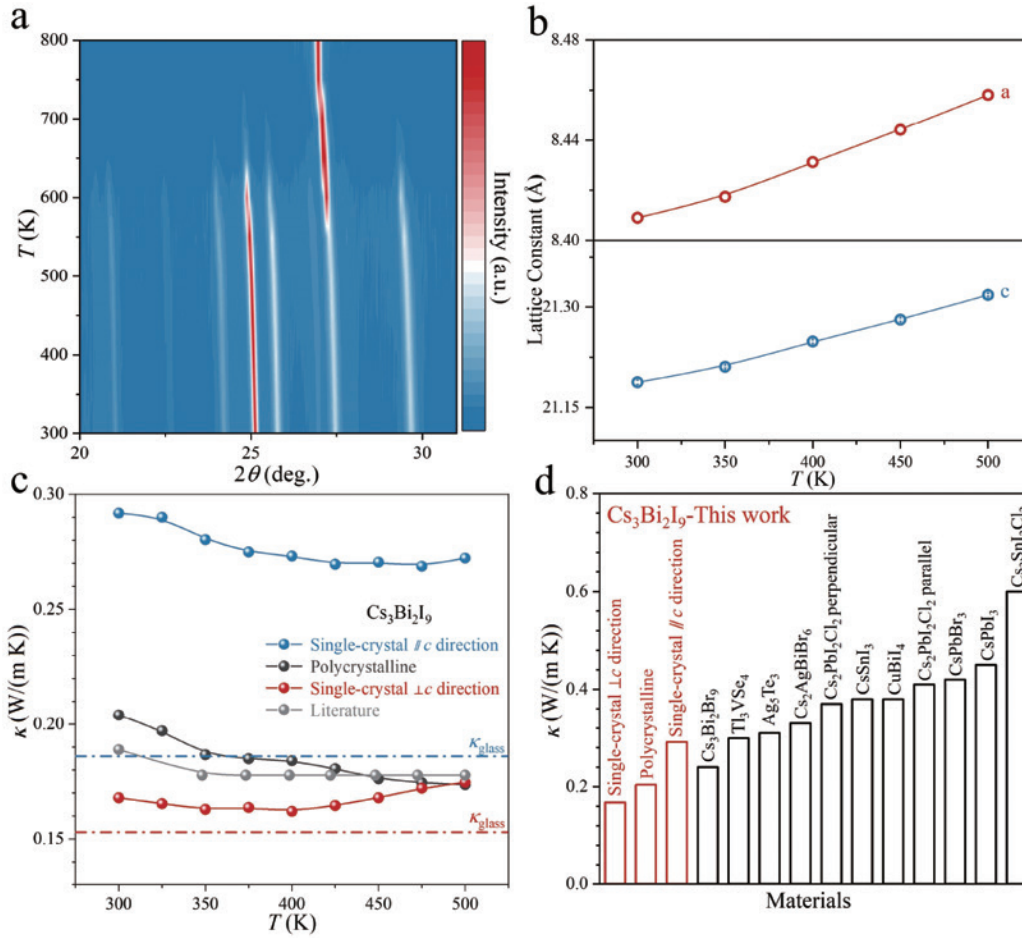
example, the formation energy of iodine vacancies (VI) in MAPbI_3 is 0.19 eV. Minns *et al.* [30] proposed that there are iodine antisite defects in MAPbI_3 . Therefore, there may also be iodine antisite defects in $\text{Cs}_3\text{Bi}_2\text{I}_9$. In addition, $\text{Cs}_3\text{Bi}_2\text{I}_9$ is a vacancy-ordered perovskite, and the vacancy at the A site (i.e., the Cs site) leads to a reduction in structural dimensionality. Thus, it may also contain cesium vacancies. These point defects can lead to broadening of the rocking curves, thereby indicating lower single-crystal quality.

An optical image of the single crystal is provided in the inset of Figure 2b. Additionally, scanning electron microscope (SEM) images and the elemental analysis further confirm the phase purity and homogeneity, as shown in Figure 2c. These features provide the data for evaluating the quality of the single crystal.

The temperature-dependent XRD results for polycrystalline $\text{Cs}_3\text{Bi}_2\text{I}_9$ are shown in Figure 3a. As the temperature increases, the diffraction peaks shift to the left. The experimental results reveal incipient decomposition of the sample above 550 K. The changes in the lattice constants are illustrated in Figure 3b, indicating positive thermal expansion behavior. The thermal expansion coefficients are consistent with those reported in the literature [31]. Lattice expansion behavior reflects the lattice anharmonicity, which leads to the enhanced phonon-phonon scattering for the reduction of thermal conductivity [32].

Figure 3c presents the temperature-dependent thermal conductivity for both single-crystalline and polycrystalline samples. The polycrystalline data agree well with the previously reported values [15]. Notably, the anisotropy in thermal transport exhibits a κ of 0.29 W/(m K) parallel to the c -direction and a κ of 0.17 W/(m K) perpendicular to the c -direction. Within the temperature range from 300 to 500 K, the thermal conductivity parallel to the c -direction gradually decreases with increasing temperature, exhibiting weak temperature dependence, which is commonly observed in disordered or complex materials [33,34]. Based on the Cahill model [35], the amorphous-limit lattice thermal conductivity parallel to the c -direction is estimated to be 0.18 W/(m K), nearly half of the measured thermal conductivity, indicating the dominant particle-like thermal transport. This is the result of the high sound velocity (discussed later) parallel to the c -direction, due to the strong binding forces between the face-sharing $[\text{CsI}_{12}]$ cuboctahedrons and $[\text{BiI}_6]$ octahedrons.

In contrast, the measured thermal conductivity perpendicular to the c -direction increases at elevated temperatures, approaching the amorphous-limit estimation of ~ 0.15 W/(m K). This indicates that the thermal



transport is primarily dominated by a wave-like mechanism, which suggests that the mean free path of phonons is below the Ioffe-Regel limit (i.e., shorter than the interatomic spacing). In terms of the lattice dynamics, the ultralow thermal conductivity of $\text{Cs}_3\text{Bi}_2\text{I}_9$ mainly originates from Cs-related low-frequency optical phonon and their overlapping transport. The relatively large values of the refined anisotropic atomic displacement parameters (U) for Cs_{2b} atoms (Table 1) indicate the presence of significant weak rattling behavior associated with the Cs–I bonds around Cs atoms. This characteristic may facilitate the generation of relatively abundant low-frequency phonons and promote the coherent propagation of phonons. The theoretical calculations of the phonon spectrum and density of states indicate that Cs-related low-frequency optical phonons indeed exist [15]. The weak rattling behavior in corner-sharing $[\text{CsI}_{12}]$ cuboctahedrons and localized rattling motion of Cs_{2b} atoms indicate predominantly wave-like transport perpendicular to the c -direction. Comparative analysis with conventional thermal insulating materials (Figure 3d) identifies that $\text{Cs}_3\text{Bi}_2\text{I}_9$ possesses the lowest thermal conductivity among the studied systems.

Figure 4a presents the sound velocities of polycrystalline and single-crystalline $\text{Cs}_3\text{Bi}_2\text{I}_9$, including the transverse (v_t), longitudinal (v_l), and average sound velocities (v_s). The relatively low sound velocity values

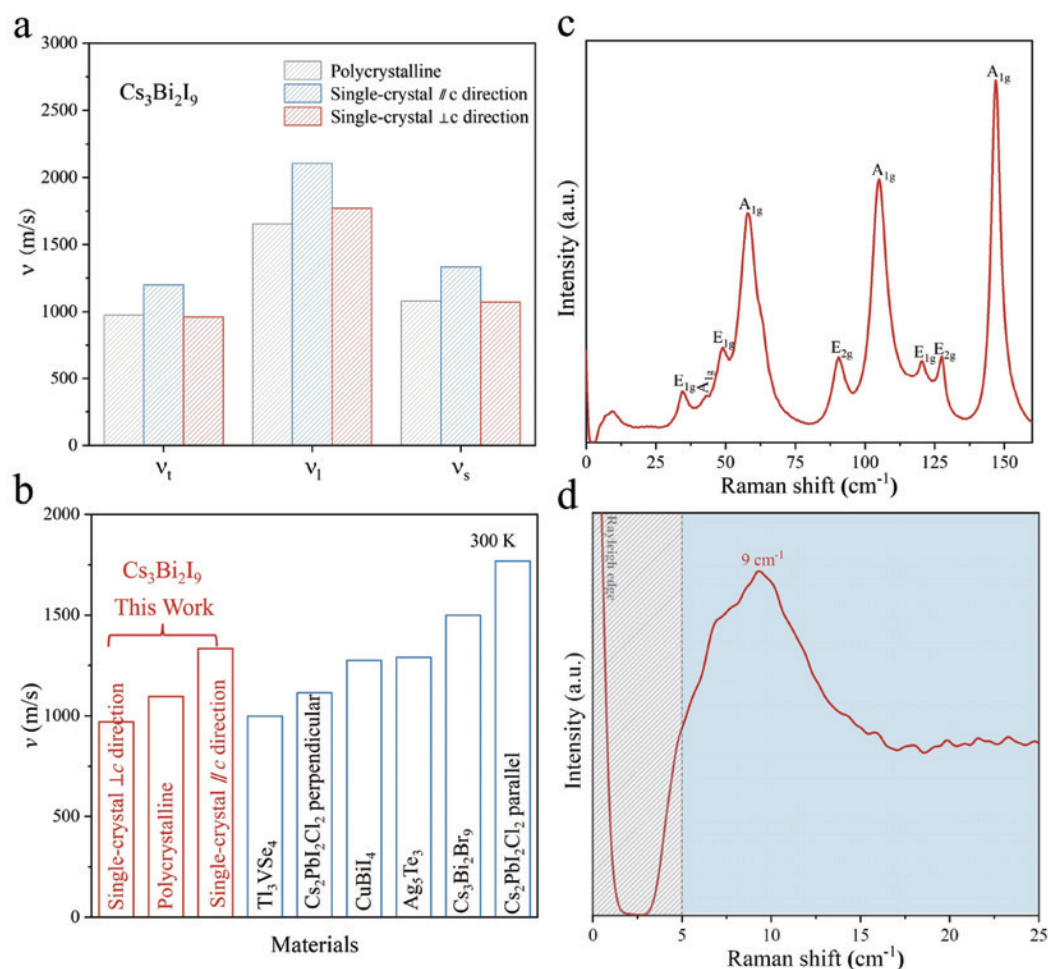


Figure 4 (a) Room-temperature sound velocity for single-crystal and polycrystalline $\text{Cs}_3\text{Bi}_2\text{I}_9$. (b) The comparison of sound velocity in thermal insulating materials [6,15,26,36,37,39]. Room-temperature Raman spectra (c) and the enlarged view (d) for single-crystal $\text{Cs}_3\text{Bi}_2\text{I}_9$.

indicate the overall weak chemical bonds, which suppress thermal propagation and ultimately lead to the ultralow thermal conductivity [41,42]. Along the c -direction, the distortion of the $[\text{Bi}_2\text{I}_9]^{3-}$ bioctahedra increases atomic disorder, reducing the transverse sound velocity. However, in polycrystalline $\text{Cs}_3\text{Bi}_2\text{I}_9$, this effect is averaged out due to the random orientations of individual grains. Consequently, the transverse sound velocity in polycrystalline $\text{Cs}_3\text{Bi}_2\text{I}_9$ falls between the values observed in single crystals for sound velocity parallel and perpendicular to the c -direction.

In single-crystalline $\text{Cs}_3\text{Bi}_2\text{I}_9$, the strong binding forces between face-sharing $[\text{CsI}_{12}]$ cuboctahedrons and $[\text{BiI}_6]$ octahedrons induce the high sound velocity parallel to the c -direction, while the weak rattling effect in corner-sharing $[\text{CsI}_{12}]$ cuboctahedrons and localized rattling motion of Cs_{2b} atoms result in the low sound velocity perpendicular to the c -direction. This observation is consistent with the nanoindentation measurements on the cleavage (00L) lattice plane. It is revealed that the elastic modulus of 11.6 GPa perpendicular to the c -direction (approximately) is responsible for the low sound velocity. The average sound velocity of $\text{Cs}_3\text{Bi}_2\text{I}_9$ is much lower compared to that of other thermal insulating materials (Figure 4b). Table 2 summarizes and compares the elastic properties based on polycrystalline and single-crystalline $\text{Cs}_3\text{Bi}_2\text{I}_9$.

Table 2 Room temperature transverse (v_t), longitudinal (v_l), and mean (v_s) sound velocities, bulk (B), shear (G), and elastic (E) moduli, Poisson ratio (r), Gruneisen parameter (γ), as well as Debye temperature (Θ_D) for polycrystalline and single-crystalline $\text{Cs}_3\text{Bi}_2\text{I}_9$

Sample	v_t (m/s)	v_l (m/s)	v_s (m/s)	B (GPa)	G (GPa)	E (GPa)	r	γ	Θ_D (K)	κ (W/(m K))
Polycrystalline	975	1655	1080	7.2	4.6	11.4	0.23	1.4	89	0.20
Single-crystal // c direction	1200	2105	1334	12.4	7.1	18.0	0.26	1.5	110	0.29
Single-crystal $\perp c$ direction	962	1770	1073	8.9	4.4	11.2	0.29	1.7	87	0.17

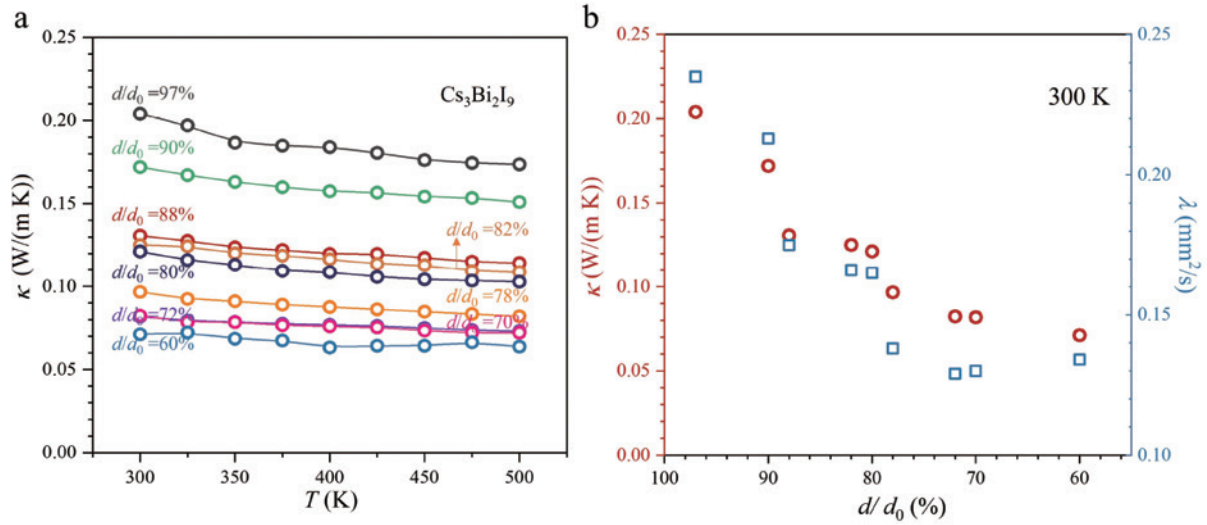


Figure 5 (a) Temperature-dependent thermal conductivity curves of $\text{Cs}_3\text{Bi}_2\text{I}_9$ polycrystalline for different relative densities. (b) Relative density-dependent thermal diffusivity and thermal conductivity of $\text{Cs}_3\text{Bi}_2\text{I}_9$ at 300 K.

The hexagonal phase exhibits pronounced anisotropy in elastic properties, where the sound velocity, modulus, and thermal conductivity parallel to the c -direction are much higher than those perpendicular to the c -direction. Additionally, the higher Gruneisen parameters (γ) correspond to the stronger anharmonic effects and increased phonon scattering.

In addition, a room-temperature Raman spectrum for the single crystal was performed using a 633 nm laser excitation source. Figure 4c shows the characteristic Raman-active modes in the wavenumber range from 25 to 150 cm^{-1} . Notably, we have experimentally observed previously unreported Raman activity below 25 cm^{-1} , which may correspond to low-frequency vibrational modes. As shown in Figure 4d, the enlarged Raman spectra in the 5–25 cm^{-1} range reveal a prominent peak at 9 cm^{-1} accompanied by multiple weaker signals between 15–25 cm^{-1} . These observed vibrational features prove the previously predictions for dynamics of corner-sharing $[\text{CsI}_{12}]$ cuboctahedrons and localized rattling motion of Cs_{26} atoms [15,17].

The temperature-dependent thermal conductivity of polycrystalline $\text{Cs}_3\text{Bi}_2\text{I}_9$ samples was systematically investigated for different relative densities, as shown in Figure 5. It is obvious that the relative density has a significant impact on the κ of $\text{Cs}_3\text{Bi}_2\text{I}_9$. When the material's relative density (d/d_0 , in which d is the measured volume density and d_0 is the theoretical volume density of 5 g/cm^3) decreases from 97% to 60%, the κ substantially decreases (Figure 5a). The reduction in thermal conductivity with decreasing density is consistent with previous reports [43]. Nine distinct density porous samples were synthesized by controlling the hot-pressing pressures and sintering temperatures. It is revealed that the room-temperature thermal con-

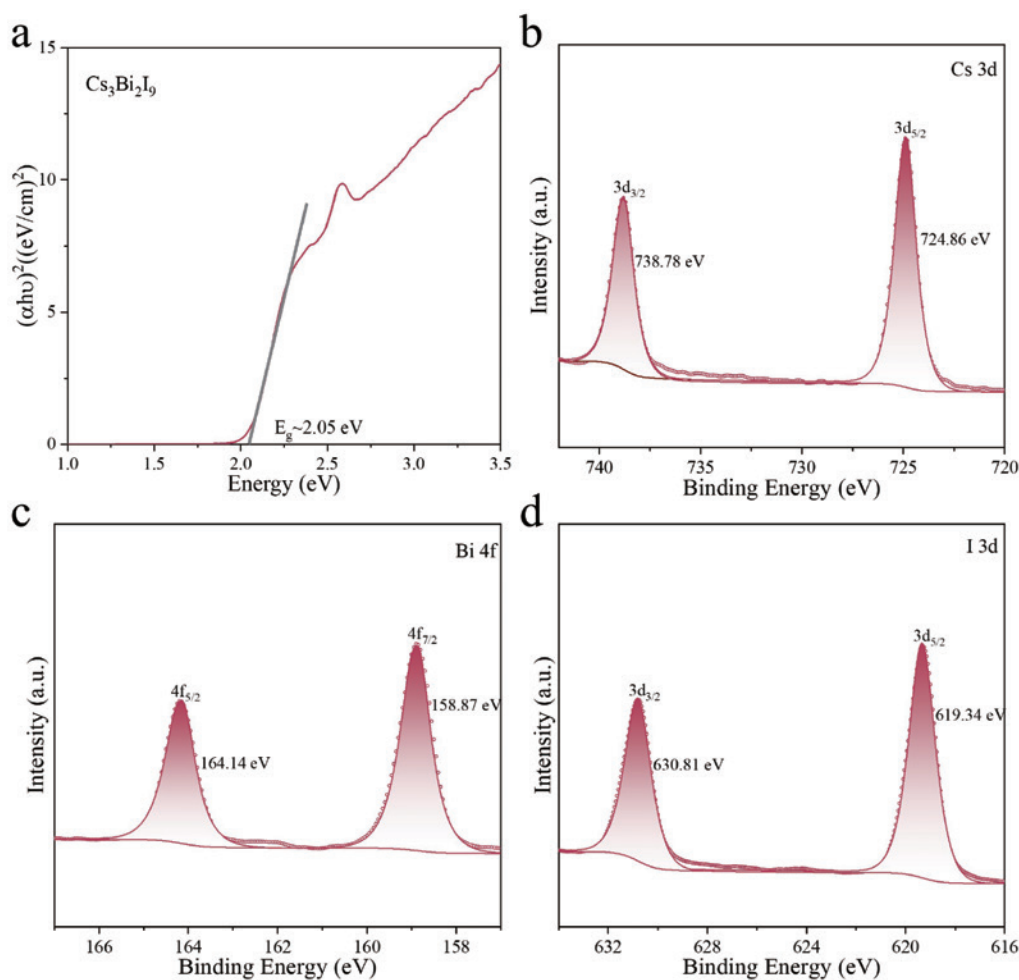


Figure 6 (a) Optical absorption spectra of $\text{Cs}_3\text{Bi}_2\text{I}_9$. X-ray photoelectron spectroscopy of $\text{Cs}_3\text{Bi}_2\text{I}_9$ (a), Cs 3d (b), Bi 4f (c), and I 3d (d).

ductivity and thermal diffusivity exhibit negative temperature dependence. Particularly, the samples with 60% relative density show a remarkably low thermal conductivity of 0.07 W/(m K) (Figure 5b). This density-dependent thermal transport behavior suggests the enhanced phonon scattering at internal pores and lattice defects in the material with low-density configurations [44,45].

The room-temperature optical bandgap of $\text{Cs}_3\text{Bi}_2\text{I}_9$ was determined through ultraviolet-visible (UV-vis) diffuse reflectance spectroscopy. The absorption spectrum reveals an absorption edge at ~ 2.05 eV with a distinct excitonic transition near 2.6 eV (Figure 6a). The bandgap width measured in this work is consistent with literature reports [15,31,46]. X-ray photoelectron spectroscopy (XPS) analysis was further conducted to probe the surface valence states of the sample. All spectra were charge-corrected using the C 1s peak at 284.8 eV as a reference. In Figure 6b, the Cs $3d_{5/2}$ and Cs $3d_{3/2}$ peaks at 724.86 and 738.78 eV, verifying the presence of Cs^+ . The +1 oxidation state of cesium reflects its strong metallic character, demonstrating that Cs tends to form ionic bonds. Figure 6c displays the Bi $4f_{7/2}$ and Bi $4f_{5/2}$ peaks, confirming Bi^{3+} states, consistent with literature [47]. Deconvolution of the I 3d doublet in Figure 6d reveals I $3d_{5/2}$ (619.34 eV) and I $3d_{3/2}$ (630.81 eV) components, demonstrating the existence of I^- [48].

Table 3 The hot-pressing parameters for obtaining polycrystalline Cs₃Bi₂I₉ with different density method

	Temperature (K)	Pressure (MPa)	Time (min)	d/d_0 (%)
Hot-pressing	500	60	40	97
Hot-pressing	500	45	30	90
Hot-pressing	500	30	20	88
Hot-pressing	500	20	10	82
Hot-pressing	500	10	5	80
Hot-pressing	450	10	5	79
Hot-pressing	400	10	5	72
Hot-pressing	350	10	5	70
Hot-pressing	300	10	5	60

CONCLUSIONS

In summary, we synthesized polycrystalline Cs₃Bi₂I₉ samples using the high-temperature melting method and grew single crystals via the vertical gradient freezing method. The material exhibits distinct thermal conductivity values along different crystallographic axes, approximately 0.29 W/(m K) parallel to the *c*-direction and 0.17 W/(m K) perpendicular to the *c*-direction. The strong binding forces between the face-sharing [CsI₁₂] cuboctahedrons and [BiI₆] octahedrons facilitate the particle-like transport parallel to the *c*-direction, while the weak rattling behavior in corner-sharing [CsI₁₂] cuboctahedrons and localized rattling motion of Cs_{2b} atoms indicate predominantly wave-like transport perpendicular to the *c*-direction. These findings provide a design principle for manipulating thermal transport through crystal chemistry engineering, opening avenues for developing anisotropic thermoelectric materials with thermal management capabilities.

METHODS

The high-purity CsI (99.9%, Aladdin) and BiI₃ (98%, Aladdin) with a stoichiometric mixture were loaded and sealed in the quartz ampules under high vacuum. For the synthesis of polycrystalline Cs₃Bi₂I₉, the ampule was heated up to 973 K and held for 6 h, and then quenched in cold water, followed by annealing at 550 K for 48 h. The resulting ingot was hand-ground into fine powder for hot pressing at 500 K for 40 min under a uniaxial pressure of 60 MPa. The dense pellets were obtained (>97% of the theoretical density), which were further fabricated with various geometries for different measurements. Polycrystalline pellets with varying densities were obtained through the hot-pressing method, and the corresponding hot-pressing conditions required to achieve specific densities are listed in Table 3.

A vertical gradient freezing method was used for the growth of single-crystal Cs₃Bi₂I₉. The ampoule was placed in a vertical temperature gradient furnace, and the temperature (T_0) located at the tip of the ampoule was heated to 973 K and held at this temperature for 10 h. From 973 to 733 K, the ampoule was slowly cooled down at a rate of ~2 K/h, and then slowly cooled to room temperature at a cooling rate of 10 K/h.

The phase composition of the pellets was examined by XRD (DX-2700) using Cu K α radiation ($\lambda=1.5406$ Å). The 2θ angle range was set from 10° to 90°, with a step size of 0.02° and an exposure time of 0.60 s per step. Temperature-dependent XRD (Rigaku SmartLab, Cu-K α radiation) of Cs₃Bi₂I₉ powders

shows no phase transition or phase decomposition up to 500 K. The diffraction data of single crystals were collected by a single crystal X-ray diffractometer (Bruker D8 VENTURE diffractometer with a PHOTON II CCD detector, Mo-K α radiation). The crystal was maintained at 300 K during data collection.

The microstructure and element distribution were confirmed using a scanning electron microscope (SEM, Phenom Pro) equipped with an energy dispersive spectrometer (EDS). Room temperature Raman spectra of Cs₃Bi₂I₉ were measured in the back-scattering configuration using a Jobin-Yvon HR800 Raman system. The instrument was equipped with a liquid nitrogen-cooled CCD detector, a 100 \times objective lens (numerical aperture, NA=0.90), and a 1800 lines/mm grating. A He-Ne laser operating at 633 nm excitation wavelength was employed, with plasma lines removed from the laser signals using BragGrate Bandpass filters. Three BragGrate notch filters (OptiGrate Corp.), each exhibiting an optical density of 4 and a FWHM of 5 cm⁻¹ [49], enabled measurements down to 5 cm⁻¹ for each excitation. To minimize sample heating effects, the laser power was maintained at approximately 50 μ W during measurements. The sound velocity was measured using a pulse receiver (Olympus-NDT) equipped with an oscilloscope (Keysight). The optical band gap was measured by UV-3600 Plus (Shimadzu). XPS (Al-K α radiation) was conducted with ESCALAB 250Xi (Thermo Fisher Scientific). Cs₃Bi₂I₉ single crystal with dimensions of 6 mm \times 5 mm was selected for the experiment. The sample was secured to the sample stage using rosin. A Nano Indenter G200 system equipped with a diamond Berkovich tip was employed for nanoindentation measurements. The maximum indentation depth was set to 500 nm. To minimize sampling bias, seven randomly distributed locations were selected for testing. The average group velocity from the nanoindentation experiment was calculated with $v_m=(v_l+2v_t)/3$, where v_t represents the transverse sound velocity.

In the temperature range from 300 to 500 K, κ was measured by the laser flash method (Netzsch LFA467) via $\kappa=\rho C_p \lambda$, where ρ is the density, C_p is the heat capacity (using the Dulong-Petit limit of heat capacity in this work, about 0.178 J/(g K) [15]), and λ is the thermal diffusivity. All samples were \sim 1.2 mm thick and tested in an argon atmosphere.

Data availability

The original data are available from corresponding authors upon reasonable request.

Acknowledgements

This work was supported by the Instrument Analysis Center of Tongji University. We thank Dr. Cheng Xu at Tongji University for the crystal structure refinement.

Funding

This work was supported by the National Key Research and Development Program of China (2022YFA1203600), the National Natural Science Foundation of China (T2125008, 92263108 and 92163203), the Shanghai Rising-Star Program (23QA1409300), and the Innovation Program of Shanghai Municipal Education Commission (202101-07-00-07-E00096).

Author contributions

Y.P., J.L. and Z.C. directed the research. L.W. performed the sample synthesis and thermal transport property measurements. Q.B., Z.L., Y.C., T.K. and C.L. analyzed the results. H.B., Z.C., J.L. and Y.P. supervised the experiment. L.W., Z.C., J.L. and Y.P. drafted the manuscript with contributions from the other authors.

Conflict of interest

The authors declare no conflict of interest.

Supplementary information

The supporting information is available online at <https://doi.org/10.1360/nso/20250056>. The supporting materials are published as submitted, without typesetting or editing. The responsibility for scientific accuracy and content remains entirely with the authors.

References

- 1 Pop E, Sinha S, Goodson KE. Heat generation and transport in nanometer-scale transistors. *Proc IEEE* 2006; **94**: 1587–1601.
- 2 Ahmed HU, Faraj RH, Hilal N, *et al.* Use of recycled fibers in concrete composites: A systematic comprehensive review. *Compos Part B-Eng* 2021; **215**: 108769.
- 3 Okamoto H, Takahashi Y, Nakamura T, *et al.* Fresnoite-type $\text{Ba}_2\text{TiGe}_2\text{O}_8$ glass-ceramics toward electro-optic device: Crystallization structure and Pockels effect. *J Eur Ceramic Soc* 2020; **40**: 5576–5581.
- 4 Cahill DG, Braun PV, Chen G, *et al.* Nanoscale thermal transport. II. 2003–2012. *Appl Phys Rev* 2014; **1**: 011305.
- 5 Lin S, Li W, Li S, *et al.* High thermoelectric performance of Ag_9GaSe_6 enabled by low cutoff frequency of acoustic phonons. *Joule* 2017; **1**: 816–830.
- 6 Acharyya P, Ghosh T, Pal K, *et al.* Intrinsically ultralow thermal conductivity in ruddlesden-popper 2D perovskite $\text{Cs}_2\text{PbI}_2\text{Cl}_2$: Localized anharmonic vibrations and dynamic octahedral distortions. *J Am Chem Soc* 2020; **142**: 15595–15603.
- 7 Lee W, Li H, Wong AB, *et al.* Ultralow thermal conductivity in all-inorganic halide perovskites. *Proc Natl Acad Sci USA* 2017; **114**: 8693–8697.
- 8 Jin H, Li J, Iocozzia J, *et al.* Hybrid organic-inorganic thermoelectric materials and devices. *Angew Chem Int Ed* 2019; **58**: 15206–15226.
- 9 Shi XL, Li NH, Li M, *et al.* Toward efficient thermoelectric materials and devices: Advances, challenges, and opportunities. *Chem Rev* 2025; **125**: 7525–7724.
- 10 Cao J, Xiong X, Zhou J. Two-dimensional lead-free mixed-halide perovskites with tunable optical properties. *J Mater Chem C* 2023; **11**: 2764–2770.
- 11 Bibi A, Lee I, Nah Y, *et al.* Lead-free halide double perovskites: Toward stable and sustainable optoelectronic devices. *Mater Today* 2021; **49**: 123–144.
- 12 Acharyya P, Ghosh T, Pal K, *et al.* Glassy thermal conductivity in $\text{Cs}_3\text{Bi}_2\text{I}_6\text{Cl}_3$ single crystal. *Nat Commun* 2022; **13**: 5053.
- 13 Bhui A, Ghosh T, Pal K, *et al.* Intrinsically low thermal conductivity in the n-type vacancy-ordered double perovskite Cs_2SnI_6 : Octahedral rotation and anharmonic rattling. *Chem Mater* 2022; **34**: 3301–3310.
- 14 Chen Z, Liu W, Shan B, *et al.* Analytical approach to structural chemistry origins of mechanical, acoustical and thermal properties. *Natl Sci Rev* 2024; **11**: nwae269.
- 15 Acharyya P, Pal K, Ahad A, *et al.* Extended antibonding states and phonon localization induce ultralow thermal conductivity in low dimensional metal halide. *Adv Funct Mater* 2023; **33**: 2304607.
- 16 Geng H, Yao X, Tu X, *et al.* Photothermally enhanced photoresponse of bismuth halide perovskite by phonon scattering. *ACS Appl Electron Mater* 2022; **4**: 217–224.
- 17 Ma JJ, Zheng JJ, Chen Y, *et al.* Intrinsic ultralow lattice thermal conductivity in lead-free halide perovskites $\text{Cs}_3\text{Bi}_2\text{X}_9$ (X = Br, I). *Phys Chem Chem Phys* 2024; **26**: 21801–21809.
- 18 Xiong W, Huang H, Wu Y, *et al.* Decoupling ultralow coherent and particle-like phonon transport via bonding hierarchy in soft superionic crystals. *Adv Sci* 2025; **12**: e06807.

- 19 Yue J, Zheng J, Li J, *et al.* Ultralow glassy thermal conductivity and controllable, promising thermoelectric properties in crystalline o -CsCu₅S₃. *ACS Appl Mater Interfaces* 2024; acsami.4c02097.
- 20 Shen X, Ouyang N, Huang Y, *et al.* Amorphous-like ultralow thermal transport in crystalline argyrodite Cu₇PS₆. *Adv Sci* 2024; **11**: 2400258.
- 21 Peierls R. Zur kinetischen Theorie der Wärmeleitung in Kristallen. *Annalen der Physik* 1929; **395**: 1055–1101.
- 22 Allen PB, Feldman JL. Thermal conductivity of disordered harmonic solids. *Phys Rev B* 1993; **48**: 12581–12588.
- 23 Phillips JC. Topology of covalent non-crystalline solids I: Short-range order in chalcogenide alloys. *J Non-Crystalline Solids* 1979; **34**: 153–181.
- 24 Cahill DG, Pohl RO. Lattice vibrations and heat transport in crystals and glasses. *Annu Rev Phys Chem* 1988; **39**: 93–121.
- 25 Li F, Liu X, Yang J, *et al.* Long-range anion correlations mediating dynamic anharmonicity and contributing to glassy thermal conductivity in well-ordered K₂Ag₄Se₃. *Small* 2025; **21**: 2409524.
- 26 Li Y, Li X, Wei B, *et al.* Phonon coherence in bismuth-halide perovskite Cs₃Bi₂Br₉ with ultralow thermal conductivity. *Adv Funct Mater* 2024; **34**: 2411152.
- 27 Chen Y, Zhou Z, Zhang B, *et al.* Lattice overdamping induced anisotropy decoupling of phonon and carrier transports in quasi-1D KCu₇S₄ textured materials. *Adv Funct Mater* 2025; **35**: 2503765.
- 28 Arakcheeva AV, Bonin M, Chapuis G, *et al.* The phases of Cs₃Bi₂I₉ between RT and 190 K. *Zeitschrift für Kristallographie - Crystalline Materials* 1999; **214**: 279–283.
- 29 Xu N, Qi X, Shen Z, *et al.* Point defects in metal halide perovskites. *Nat Rev Phys* 2025; **7**: 554–564.
- 30 Minns JL, Zajdel P, Chernyshov D, *et al.* Structure and interstitial iodide migration in hybrid perovskite methylammonium lead iodide. *Nat Commun* 2017; **8**: 15152.
- 31 McCall KM, Stoumpos CC, Kostina SS, *et al.* Strong electron-phonon coupling and self-trapped excitons in the defect halide perovskites A₃M₂I₉ (A = Cs, Rb; M = Bi, Sb). *Chem Mater* 2017; **29**: 4129–4145.
- 32 Lu H, Zhou C, Song Y, *et al.* A strategy to reduce thermal expansion and achieve higher mechanical properties in iron alloys. *Nat Commun* 2025; **16**: 211.
- 33 Brown SR, Kauzlarich SM, Gascoin F, *et al.* Yb₁₄ MnSb₁₁: New high efficiency thermoelectric material for power generation. *Chem Mater* 2006; **18**: 1873–1877.
- 34 Ren Q, Gupta MK, Jin M, *et al.* Extreme phonon anharmonicity underpins superionic diffusion and ultralow thermal conductivity in argyrodite Ag₈SnSe₆. *Nat Mater* 2023; **22**: 999–1006.
- 35 Agne MT, Hanus R, Snyder GJ. Minimum thermal conductivity in the context of diffusion-mediated thermal transport. *Energy Environ Sci* 2018; **11**: 609–616.
- 36 Mukhopadhyay S, Parker DS, Sales BC, *et al.* Two-channel model for ultralow thermal conductivity of crystalline Tl₃VSe₄. *Science* 2018; **360**: 1455–1458.
- 37 Zhang X, Chen Z, Lin S, *et al.* Promising thermoelectric Ag_{5-δ}Te₃ with intrinsic low lattice thermal conductivity. *ACS Energy Lett* 2017; **2**: 2470–2477.
- 38 Klarbring J, Hellman O, Abrikosov IA, *et al.* Anharmonicity and ultralow thermal conductivity in lead-free halide double perovskites. *Phys Rev Lett* 2020; **125**: 045701.
- 39 Das A, Pal K, Acharyya P, *et al.* Strong antibonding I (p)–Cu (d) states lead to intrinsically low thermal conductivity in CuBi₄. *J Am Chem Soc* 2023; **145**: 1349–1358.
- 40 Zeng Z, Chen C, Zhang C, *et al.* Critical phonon frequency renormalization and dual phonon coexistence in layered Ruddlesden-Popper inorganic perovskites. *Phys Rev B* 2022; **105**: 184303.
- 41 Li W, Lin S, Ge B, *et al.* Low sound velocity contributing to the high thermoelectric performance of Ag₈SnSe₆. *Adv Sci* 2016; **3**: 1600196.
- 42 Ma N, Zhang Z, Nan P, *et al.* Phonon symphony of stacked multilayers and weak bonds lowers lattice thermal conductivity. *Adv Mater* 2022; **34**: 2202677.
- 43 Wu L, Zhang X, Li C, *et al.* Thermal transport properties of polycrystalline Bi₄SeCl₂O₄ with various texturizations and

- densities. *Mater Today Phys* 2025; **50**: 101618.
- 44 Lee H, Vashaee D, Wang DZ, *et al.* Effects of nanoscale porosity on thermoelectric properties of SiGe. *J Appl Phys* 2010; **107**: 094308.
- 45 Khan AU, Kobayashi K, Tang DM, *et al.* Nano-micro-porous skutterudites with 100% enhancement in ZT for high performance thermoelectricity. *Nano Energy* 2017; **31**: 152–159.
- 46 Gu J, Yan G, Lian Y, *et al.* Bandgap engineering of a lead-free defect perovskite Cs₃Bi₂I₉ through trivalent doping of Ru³⁺. *RSC Adv* 2018; **8**: 25802–25807.
- 47 Tang H, Wang X, Yao C, *et al.* 0D/3D heterostructure of perovskite Cs₂CuBr₄ quantum dots/Bi₂O₃ microflower as a step-scheme photocatalyst for enhanced CO₂ reduction. *Sep Purif Technol* 2024; **338**: 126544.
- 48 Bai Y, Ye L, Wang L, *et al.* g-C₃N₄/Bi₄O₅I₂ heterojunction with I³⁻/I⁻ redox mediator for enhanced photocatalytic CO₂ conversion. *Appl Catal B-Environ* 2016; **194**: 98–104.
- 49 Tan PH, Han WP, Zhao WJ, *et al.* The shear mode of multilayer graphene. *Nat Mater* 2012; **11**: 294–300.